Polarization-Independent Nonreciprocal Narrowband and Wide-angle Thermal Emission based on Rotated Weyl Semimetals

Cailing Huang(黄彩玲) [1], Kaixing Chen(陈凯星) [2], Hailun Li(李海伦) [1], Kezhang Shi(史可樟) [3,4,5*] and Chengping Yin(尹承平) [1*]

1 Key Laboratory of Atomic and Subatomic Structure and Quantum Control (Ministry of Education), School of Physics, Guangdong Provincial Key Laboratory of Quantum Engineering and Quantum Materials, Guangdong-Hong Kong Joint Laboratory of Quantum Matter, Frontier Research Institute for Physics, South China Normal University, Guangzhou 510006, China

2 Centre for Optical and Electromagnetic Research, ZJU-SCNU Joint Center of Photonics, South China Academy of Advanced Optoelectronics, South China Normal University, Guangzhou 510006, China

3 Ningbo Global Innovation Center, Zhejiang University, Ningbo 315100, China

4 Centre for Optical and Electromagnetic Research, National Engineering Research Center for Optical Instruments, Zhejiang University, Hangzhou 310058, China

5 School of Information Science and Engineering, NingboTech University, Ningbo 315100, China

*Corresponding authors Email: kezhang-shi@zju.edu.cn; yinchengping@m.scnu.edu.cn

Abstract: Nonreciprocal thermal emission significantly boosts energy conversion efficiency by enabling independent control over emissivity and absorptivity. Most existing nonreciprocal thermal emitters are limited to a single polarization, whereas realizing polarization-independent nonreciprocal emission holds even greater significance. In this work, we demonstrate a Weyl semimetal (WSM)/Si/WSM/Ag heterostructure comprising the top and bottom WSM layers rotated at distinct angles. The results demonstrate a narrowband and wide angular nonreciprocal emission with both TM and TE polarizations, exhibiting a strong nonreciprocity exceeding 0.86 at a resonant wavelength of 9.22 μm, while preserving robust angular stability ($\Delta\theta = 43°$ for TM and $\Delta\theta = 60°$ for TE). Impedance-matching analysis and field distributions elucidate the underlying physical mechanism. Furthermore, the effects of the rotation angles and the Si-layer thickness on the nonreciprocal performance are also

comprehensively analyzed. This work advances nonreciprocal thermal emitters toward higher efficiency, offering promising prospects in thermal management and thermophotovoltaics.

Keywords: Polarization-Independent, nonreciprocal thermal emission, Weyl semimetals, Fabry–Pérot resonance

PACS: 44.40.+a, 42.25.Bs

1. Introduction

Thermal emission is a fundamental physical process in which any object with a temperature above absolute zero spontaneously radiates electromagnetic energy [1-3]. Exploiting this radiative energy is pivotal for a wide spectrum of applications, encompassing radiative cooling [4,5], thermal management [6,7], infrared imaging [8], and detection systems [9]. Conventional thermal emission is largely constrained by the reciprocity constraint of Kirchhoff's law, which requires the spectral directional emissivity (e) to be strictly equal to the absorptivity (α) under thermodynamic equilibrium, i.e., $e(\lambda,\theta)=\alpha(\lambda,\theta)$. Consequently, the conversion of absorbed incident radiation into other forms of energy, such as electricity or heat, is inherently accompanied by a mandatory thermal radiation from the object at the exact same wavelength and direction [10]. Such a constraint inevitably leads to inherent energy losses and imposes a theoretical efficiency limit on energy harvesting.

Nonreciprocal thermal emission offers a vital strategy to enable thermal energy harvesting that exceeds the Shockley-Queisser limit [11,12]. State-of-the-art nonreciprocal emitters predominantly rely on magneto-optical materials like magnetized InAs/InSb and magnetic Weyl semimetals (WSMs). In these systems, nonreciprocal responses are mainly investigated in two fundamental polarization states: the transverse magnetic (TM) mode (the magnetic field is perpendicular to the plane of incidence) and the transverse electric (TE) mode (the electric field is perpendicular to the plane of incidence). Specifically, TM-polarized nonreciprocity is readily achievable through the direct coupling between the material's antisymmetric

dielectric tensor components (ε_{xz} and ε_{zx}) and the TM electric-field components (E_x and E_z) [13]. In contrast, TE modes generally reciprocal as they only contain a non-zero E_y component that cannot couple to the antisymmetric tensor components. Nevertheless, recent studies have demonstrated that TE-polarized nonreciprocity can be achieved by introducing non-zero azimuthal angles to induce polarization conversion [14-18], as well as by utilizing complex metasurfaces driven by multimode interaction [19,20].

Driven by the violation of Lorentz reciprocity via asymmetric permittivity tensors ($\varepsilon \neq \varepsilon^T$) [21], nonreciprocal thermal radiation provides a revolutionary route to break Kirchhoff's law [$e(\theta) \neq a(\theta)$]. However, most nonreciprocal thermal emitters remain limited to a single-polarization operation. Under realistic illumination conditions, where the incident radiation intrinsically contains mixed TM-polarized and TE-polarized components, single-polarization nonreciprocal emitters can harvest at most 50% of the available radiative power compared to an unpolarized counterpart [22]. Therefore, achieving a polarization-independent nonreciprocal response which simultaneously supports both TM and TE polarizations at identical wavelengths is essential to maximize overall thermal energy harvesting. Li and Zheng [23] demonstrated a polarization-independent response in an AlN/WSM/Ag planar heterostructure, but the relatively weak nonreciprocity limits the enhancement of its overall radiative performance. Fang et al. [24] proposed a structure based on twisted Weyl semimetal that excites dual-polarization nonreciprocal thermal radiation in both TE and TM modes by adjusting the positions of Weyl nodes in momentum space. However, this approach inherently relies on two independent configurations of structural parameters, making it difficult to achieve simultaneous enhancement of dual-polarization within a single structure at a single wavelength. Other unified structures have been explored for dual-polarization nonreciprocal thermal emission [13,25-31]. Nevertheless, these designs rely on complex nanofabrication and face the challenges of inconsistent resonant wavelengths or limited angular responses.

In this work, we propose a pattern-free WSM/Si/WSM/Ag Fabry–Pérot resonator designed for polarization-independent, narrowband and wide-angle nonreciprocal

thermal emission. By rotating the top and bottom WSM layers at distinct angles, the proposed structure successfully realizes the simultaneous enhancement of nonreciprocal radiation for both polarizations at the identical resonant wavelength. Furthermore, it maintains strong nonreciprocity with angular ranges of $\Delta\theta = 43°$ and $\Delta\theta = 60°$ for TM and TE modes, respectively. Impedance-matching analysis and field distribution analysis are employed to explain the physical mechanism underlying this nonreciprocal response. This work propels the development of nonreciprocal thermal emitters toward higher efficiency and paves the way for the multi-polarization utilization of radiative energy.

2. Results and discussion

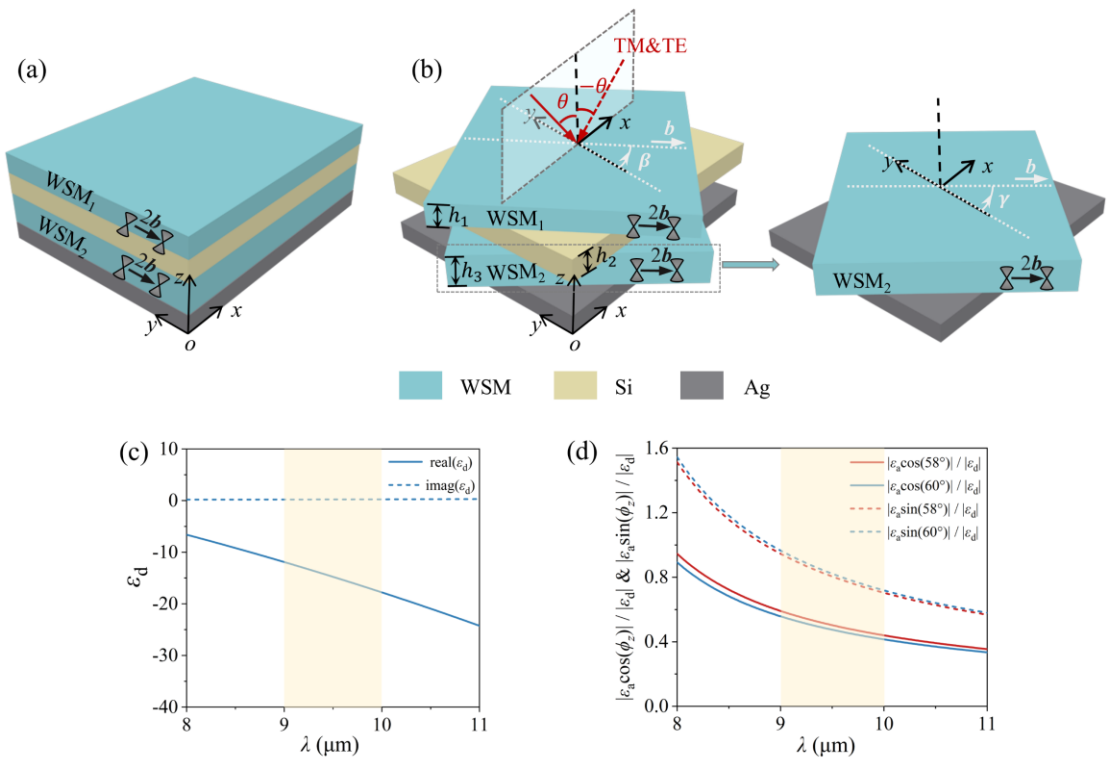


Fig. 1. (a) The planar WSM/Si/WSM/Ag structure without any rotation operations. (b) The designed polarization-independent nonreciprocal thermal emitter configuration with the top WSM layer rotated by β and the bottom WSM layer rotated by γ. The thicknesses of the first (WSM_1), second (Si), and third (WSM_2) layers are denoted as h_1, h_2 and h_3. The solid and dashed red lines denote oblique incidence at θ and $-\theta$ angles, respectively. (c) Wavelength dependence of the real (solid blue) and imaginary (dashed blue) parts of the diagonal component ε_{d}. (d) Wavelength dependence of the permittivity-components ratios $|\varepsilon_{\mathrm{a}} \cos \phi_z|/|\varepsilon_{\mathrm{d}}|$ (solid) and $|\varepsilon_{\mathrm{a}} \sin \phi_z|/|\varepsilon_{\mathrm{d}}|$ (dashed) at $\phi_z = 58°$ and $60°$. The shaded areas highlight the spectral range relevant to the thermal emitter.

The proposed polarization-independent nonreciprocal thermal emitter consists of a multi-layer thin-film system [Fig. 1(b)]: a WSM top layer of thickness h_1, a Si dielectric spacer ($\varepsilon_{\mathrm{Si}} = 11.7$) of thickness h_2, and a WSM bottom layer of thickness h_3, deposited on an Ag back reflector. Spatial symmetry is broken by applying a z-axis rotation to both WSM components, where the first and third layers are rotated

counterclockwise by β and γ, respectively.

In WSMs, accidental degeneracies known as Weyl nodes occur in pairs in the band structure and act as sources and sinks of Berry curvature [32,33]. The momentum separation between the node pair manifests as an axial vector $\boldsymbol{b}$, which acts as an internal magnetic field [34]. We choose a coordinate system in which $\boldsymbol{b}$ is aligned with the –*y*-axis, perpendicular to the incident plane (*x*-*z* plane), as shown in Fig. 1(a). In this configuration, the permittivity tensor of the WSM takes the following form [35-37]

$$\varepsilon = \begin{bmatrix} \varepsilon_{\mathrm{d}} & 0 & i\varepsilon_{\mathrm{a}} \\ 0 & \varepsilon_{\mathrm{d}} & 0 \\ -i\varepsilon_{\mathrm{a}} & 0 & \varepsilon_{\mathrm{d}} \end{bmatrix}. \tag{1}$$

When the WSM is rotated counterclockwise about the *z*-axis through an angle ϕ_z, the transformed permittivity tensor ε' is obtained using the rotation matrix M_z [13,38]:

$$\varepsilon'(\phi_z) = M_z \varepsilon M_z^{\mathrm{T}}, \tag{2}$$

where

$$M_z = \begin{bmatrix} \cos\phi_z & -\sin\phi_z & 0 \\ \sin\phi_z & \cos\phi_z & 0 \\ 0 & 0 & 1 \end{bmatrix}. \tag{3}$$

Evaluating Eq. (2) yields the generalized permittivity tensor for the rotated WSM:

$$\varepsilon'(\phi_z) = \begin{bmatrix} \varepsilon_{\mathrm{d}} & 0 & i\varepsilon_{\mathrm{a}}\cos\phi_z \\ 0 & \varepsilon_{\mathrm{d}} & i\varepsilon_{\mathrm{a}}\sin\phi_z \\ -i\varepsilon_{\mathrm{a}}\cos\phi_z & -i\varepsilon_{\mathrm{a}}\sin\phi_z & \varepsilon_{\mathrm{d}} \end{bmatrix}. \tag{4}$$

Consequently, the permittivity tensors of the top (WSM_1) and bottom (WSM_2) layers are readily obtained by setting their rotation angles to β and γ, respectively, such that $\varepsilon_{\mathrm{WSM1}} = \varepsilon'(\beta)$ and $\varepsilon_{\mathrm{WSM2}} = \varepsilon'(\gamma)$. Notably, this rotation symmetry-breaking introduces new off-diagonal components in the *y*-*z* plane (i.e., $\varepsilon_{yz}, \varepsilon_{zy} \neq 0$), thereby modifying the anisotropy of the system and inducing a nonreciprocal response under TE polarization.

The magnitudes of these off-diagonal elements are governed by ε_{a}, whereas the diagonal elements are characterized by ε_{d}, with:

$$\varepsilon_{\mathrm{a}} = \frac{be^2}{2\pi^2\hbar\omega\varepsilon_0}, \tag{6}$$

$$\varepsilon_{\mathrm{d}} = \varepsilon_{\mathrm{b}} + i\frac{\sigma}{\Omega_0}, \tag{7}$$

where ε_0 is the vacuum permittivity, ε_{b} represents the background permittivity, and $\Omega_0 = \hbar\omega/E_{\mathrm{F}}$ represents the normalized real frequency. The conductivity σ is given by

$$\sigma = \frac{r_{\mathrm{s}}g}{6}\Omega G\left(\frac{\Omega}{2}\right) + i\frac{r_{\mathrm{s}}g}{6\pi}\left\{\frac{4}{\Omega}\left[1 + \frac{\pi^2}{3}\left(\frac{k_{\mathrm{B}}T}{E_{\mathrm{F}}}\right)^2\right] + 8\Omega\int_0^{\xi_{\mathrm{c}}}\frac{G(\xi) - G\left(\frac{\Omega}{2}\right)}{\Omega^2 - 4\xi^2}\xi\mathrm{d}\xi\right\}. \tag{8}$$

Here, $r_{\mathrm{s}} = \frac{e^2}{(4\pi\varepsilon_0\hbar v_{\mathrm{F}})}$ is the effective fine structure constant, $\Omega = \frac{\hbar(\omega + i\tau^{-1})}{E_{\mathrm{F}}}$ is the normalized complex frequency, $n(E) = \frac{1}{e^{(E-E_{\mathrm{F}})/(k_{\mathrm{B}}T)}+1}$ is the Fermi distribution function, $G(E) = n(-E) - n(E)$. In addition, E_{F} is the chemical potential, ξ_{c} is the normalized cutoff energy, v_{F} is the Fermi velocity, g is the number of Weyl points, τ^{-1} represents the scattering rate and k_{B} is the Boltzmann constant.

Following Ref. [35], the parameters are set to $b = 2 \times 10^9\ \mathrm{m}^{-1}$, $\varepsilon_{\mathrm{b}} = 6.2$, $v_{\mathrm{F}} = 0.83 \times 10^5\ \mathrm{m/s}$, $g = 2$, $\tau = 1000\ \mathrm{fs}$, $T = 100\ \mathrm{K}$, and $\xi_{\mathrm{c}} = 3$. Since the chemical potential E_{F} can be tuned by varying the dopant species and concentration, we set $E_{\mathrm{F}} = 0.2\ \mathrm{eV}$ for both WSM_1 and WSM_2 in the present study [39-41]. In the 9–10 μm wavelength range, the diagonal elements exhibit a pronounced negative real part [Fig. 1(c)], revealing the metallic-like optical response of the Weyl semimetal. Furthermore, to quantify the excited nonreciprocal response, the ratio of off-diagonal to diagonal components at various twist angles is calculated in Fig. 1(d).

The permittivity of Ag is described by the Drude model [31]:

$$\varepsilon_{\mathrm{Ag}} = \varepsilon_\infty - \frac{{\omega_{\mathrm{p}}}^2}{\omega(\omega + i\Gamma)}. \tag{9}$$

Here, the high-frequency dielectric constant ε_∞, the scattering rate Γ and the plasma frequency ω_{p} are set to 3.4, 2.7×10^{13} rad/s and 1.39×10^{16} rad/s, respectively. Since the thickness of the Ag layer significantly exceeds its skin depth, the transmittance *T* of the planar structure can be neglected.

This work considers two polarization states: the TM and TE mode. In the local coordinate system shown in Fig. 1(b), the solid and dashed red lines represent waves incident obliquely at positive (θ) and negative ($-\theta$) angles with respect to the surface normal, respectively. For both TM and TE polarizations at a given incidence angle θ, the emissivity $e(\lambda,\theta)$ and absorptivity $\alpha(\lambda,\theta)$ of the system can be expressed in terms of its reflectivity $R(\lambda,\theta)$ as follows:

$$e(\lambda,\theta) = 1 - R(\lambda,-\theta), \tag{10}$$

$$\alpha(\lambda,\theta) = 1 - R(\lambda,\theta). \tag{11}$$

For reciprocal media, the Lorentz reciprocity theorem ensures that the reflectivity is symmetric with respect to the incidence angle, i.e., $R(\lambda,\theta) = R(\lambda,-\theta)$. Thus, the system obeys the conventional Kirchhoff's law, $e(\lambda,\theta) = \alpha(\lambda,\theta)$. In contrast, in nonreciprocal media, the permittivity tensor generally contains non-zero off-diagonal elements that break Lorentz reciprocity and give rise to an asymmetric reflection response [42]. Under these conditions, the conventional form of Kirchhoff's law no longer holds. Nevertheless, combining the above definitions shows that a well-defined relationship between emissivity and absorptivity remains valid in the nonreciprocal system, as expressed by the generalized form of Kirchhoff's law: $e(\lambda,\theta) = \alpha(\lambda,-\theta)$ [43]. The difference between the absorptivity $\alpha(\lambda,\theta)$ and the emissivity $e(\lambda,\theta)$, denoted by $\eta(\lambda,\theta)$, is defined to quantify the degree of nonreciprocity as follows:

$$\eta(\lambda,\theta) = \alpha(\lambda,\theta) - e(\lambda,\theta). \tag{12}$$

In this work, the reflectivity, emissivity and absorptivity are calculated using the rigorous coupled-wave analysis (RCWA) and further validated using the finite-element method (FEM) implemented in COMSOL Multiphysics.

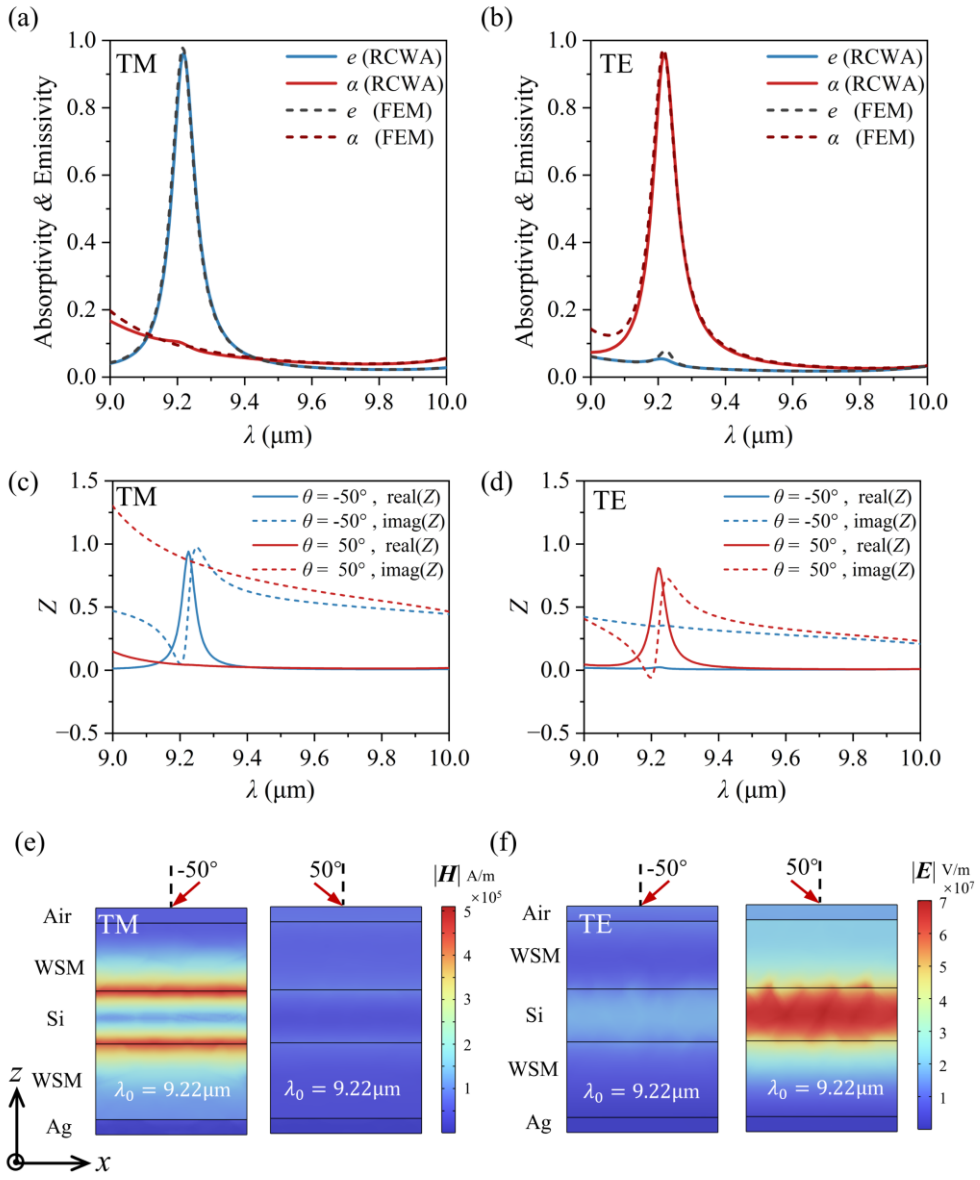


Fig. 2. The (a) TM-polarized and (b) TE-polarized absorptivity and emissivity with an incidence angle of 50°. The solid and dashed lines denote RCWA and FEM results, respectively. The (c) TM-polarized and (d) TE-polarized effective impedance. (e)-(f), Spatial distributions of the magnetic field norm $|H|$ for TM (e) and electric field norm $|E|$ for TE polarizations (f) at the incidence angle of ±50° and $\lambda_0 = 9.22\mu m$.

For the realization of efficient nonreciprocal thermal radiation with polarization independence in the mid-infrared region, the optimal parameters are set as follows:

$h_1 = 0.9\ \mu m$, $h_2 = 0.7\ \mu m$, $h_3 = 1\ \mu m$, $\beta = 58°$, $\gamma = 60°$. Specifically, the rotation angles (β and γ) were determined based on the distinct spectral responses of the TM and TE resonances to the two angles. Figs. 2(a) and 2(b) present the absorptivity and emissivity spectra at $\theta = 50°$ for TM and TE polarizations, respectively. The excellent agreement between the results obtained using the two numerical methods confirm the accuracy of the simulation. The proposed structure exhibits a pronounced nonreciprocal response at the resonant wavelength ($\lambda_0 = 9.22\mu m$), while demonstrating excellent polarization independence. Here, "polarization-independent" specifically denotes that both TM and TE polarizations achieve strong nonreciprocity at the identical resonant wavelength, while exhibiting virtually equal performance. At this resonant wavelength, the TM-polarized emissivity reaches 96.17%, whereas the corresponding absorptivity is only 9.86%. For TE polarization, the absorptivity reaches 96.06% at the same resonant wavelength, whereas the emissivity is only 5.30%. The difference in nonreciprocal efficiency between the two polarization states is thus less than 5%. This facilitates the spatial manipulation of photon transmission, such as net photon flow control in thermal circulators [25,39]. Additionally, the preferred emission directions for TM and TE polarizations are concentrated at θ and $-\theta$, respectively. This directional separation enables the two polarization channels to be collected independently, thereby avoiding cross-polarization losses and simplifying the downstream optical system [13,44]. The Q-factor ($Q = \lambda_0/\Delta\lambda$, where λ_0 is the resonant wavelength and $\Delta\lambda$ is the full width at half maximum of the spectra) is calculated to be 110 for TM mode and 106 for TE mode, indicating high frequency resolution and excellent spectral selectivity for both polarizations.

The effective impedance matching theory is employed to explain nonreciprocal phenomena, which can be expressed as follows [45,46]:

$$Z = \sqrt{\frac{(1+S_{11})^2 - S_{21}^2}{(1-S_{11})^2 - S_{21}^2}}, \tag{13}$$

where S_{11} and S_{21} denote the scattering parameters associated with reflection and

transmission coefficients, expressed as $R = |S_{11}|^2$ and $T = |S_{21}|^2$. Since the transmission is obstructed by the Ag layer, a strong absorption or emission response can be obtained by matching the effective impedance to the free-space impedance ($Z_0 = 1$), which simultaneously suppresses reflectance. Figs. 2(c) and 2(d) present the calculated effective impedances for TM and TE polarizations, respectively. Specifically, for the TM polarization at the resonant wavelength, the effective impedance at -50° incidence is $Z_{\mathrm{TM}}(-50°) = 0.8981 + 0.3175\mathrm{i}$, which is closely matched to the free-space impedance, thereby resulting in weak reflection and strong emission. In contrast, the effective impedance changes to $Z_{\mathrm{TM}}(50°) = 0.0429 + 0.8756\mathrm{i}$ at 50° incidence. This pronounced mismatch with the free-space impedance leads to strong reflection and weak absorption. Similarly, for the TE polarization, a favorable impedance match is achieved at 50° incidence [$Z_{\mathrm{TE}}(50°) = 0.8097 + 0.2719\mathrm{i}$], whereas a pronounced impedance mismatch occurs under -50° incidence [$Z_{\mathrm{TE}}(-50°) = 0.0231 + 0.3500\mathrm{i}$]. Consequently, at the resonant wavelength under 50° incidence, a pronounced absorption peak emerges, whereas the corresponding emission is almost entirely suppressed. The rotation of the WSM layers plays a crucial role in establishing these impedance-matching conditions. Each WSM layer is homogeneous and unpatterned, but its electromagnetic response is anisotropic: the permittivity tensor depends on the orientation of the Weyl-node separation vector $\boldsymbol{b}$. Rotating a WSM layer reorients $\boldsymbol{b}$ relative to the incidence plane and layer normal, and further affects the reflection coefficient (S_{11}) and phase response of the overall structure. Therefore, the rotation angles of the two WSM layers provide additional degrees of freedom to adjust the reflection phase of the multilayer cavity. By selecting the rotation angles of $\mathrm{WSM_1}$ and $\mathrm{WSM_2}$ appropriately, the impedance-matching conditions associated with the TM and TE resonances can be independently tailored and aligned at the same resonance wavelength, enabling nonreciprocal thermal radiation for both polarization states in a single structure.

To further elucidate the mechanism underlying the strong nonreciprocal response, the resonance characteristics of the structure are analyzed. The entire structure can be

regarded as a Fabry–Pérot (FP) resonator, in which the top and bottom WSM layers serve as metallic mirrors, while the intermediate Si layer acts as the cavity dielectric medium. When the cavity resonance condition is satisfied, the waves undergoing multiple reflections within the cavity interfere constructively, thereby exciting an FP resonance and producing pronounced field enhancement at the resonant wavelength. The corresponding resonance condition is given by [47]:

$$\varphi_{\mathrm{total}}(\lambda,\theta)=\varphi_{\mathrm{WSM1}}+\varphi_{\mathrm{Si}}+\varphi_{\mathrm{WSM2}}=2m\pi\ (m=0,1,2,3\ldots\ldots), \tag{14}$$

where φ_{WSM1} and φ_{WSM2} denote the reflection phase shifts at the upper (WSM_1) and lower (WSM_2) interfaces, respectively. The round-trip propagation phase shift within the Si cavity is expressed as:

$$\varphi_{\mathrm{Si}}=2k_0n_{\mathrm{Si}}h_2\cos\theta_{\mathrm{Si}}=2k_0h_2\sqrt{\varepsilon_{\mathrm{Si}}-(\sin\theta)^2}. \tag{15}$$

Here, $k_0=2\pi/\lambda$ is wavevector in free space, $n_{\mathrm{Si}}=\sqrt{\varepsilon_{\mathrm{Si}}}$ and h_2 are the refractive index and thickness of the Si layer, respectively, θ is the incident angle in air, and θ_{Si} is the refraction angle inside the Si cavity satisfying Snell's law ($n_{\mathrm{air}}\sin\theta=n_{\mathrm{Si}}\sin\theta_{\mathrm{Si}}$).

The corresponding spatial distributions of the magnetic field norm $|H|$ for TM and electric field norm $|E|$ for TE polarizations at the resonant wavelength are illustrated in Figs. 2(e) and 2(f), respectively. Under TM-polarized incidence at -50°, the FP resonance is excited, producing a standing-wave pattern with pronounced $|H|$ antinodes near the Si/WSM interfaces and field penetration to the Si cavity. Such FP resonant enable high emissivity. By contrast, at 50° incidence, the magnetic field throughout the entire structure remains extremely weak, indicating that the FP resonance mode is not excited. Thus, the incident wave fails to enter the cavity, resulting in low absorptivity. Similarly, under TE-polarized incidence, the electric field is strongly confined within the cavity at an incidence angle of 50° to enable high absorptivity, whereas it is strongly suppressed at -50° incidence, resulting in low emissivity.

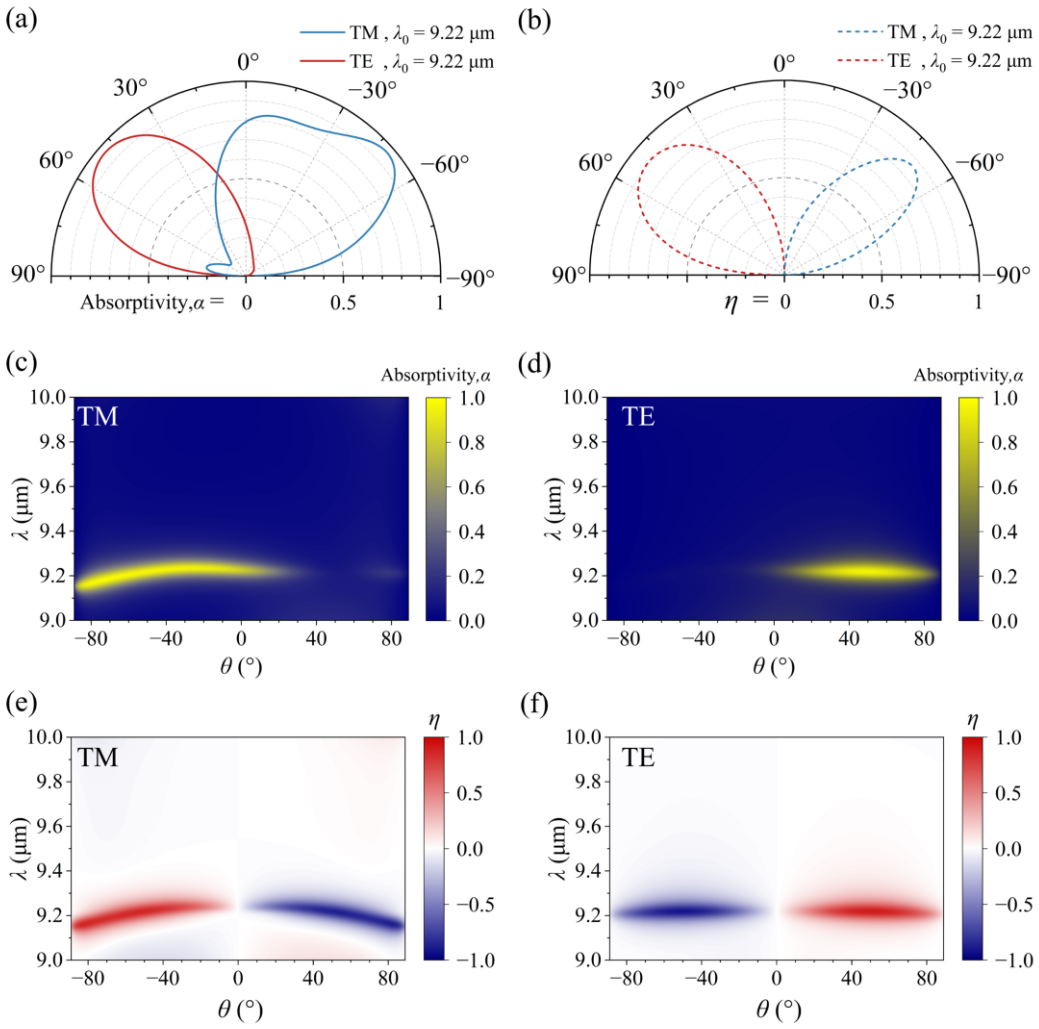


Fig. 3. Angular (a) absorption and (b) nonreciprocity profile at $\lambda_0 = 9.22\mu m$ displayed in polar coordinates. The blue and red (dashed) lines correspond to TM and TE polarizations, respectively. Absorptivity color maps for (c) TM and (d) TE polarizations. Nonreciprocity color maps for (e) TM and (f) TE polarizations.

Figures. 3(a) and 3(b) present the angular absorption and nonreciprocity profiles in polar coordinates at the resonant wavelength. Notably, both polarizations simultaneously exhibit high absorptivity (emissivity) and pronounced nonreciprocal thermal radiation over broad angular ranges. Specifically, the TM polarization maintains a high absorptivity $[\alpha(\lambda, -\theta) > 0.5]$ over a wide angular range from 0° to –77°. However, due to the presence of residual absorption at positive angles, the

angular window for sustaining a high nonreciprocity [$\eta(\lambda, -\theta) > 0.5$] is confined to $-26° \sim -69°$ ($\Delta\theta = 43°$). In contrast, the TE polarization exhibits superior performance, achieving $\alpha(\lambda, \theta) > 0.5$ between 14° to 79°. Crucially, the near-complete suppression of absorptivity at negative angles extends the high-nonreciprocity [$\eta(\lambda, \theta) > 0.5$] angular range to $19° \sim 79°$ ($\Delta\theta = 60°$).

To comprehensively characterize the angular response and absorption characteristics, the absorptivity maps for both TM and TE polarizations are shown in Figs. 3(c) and 3(d), respectively. The yellow bands, which correspond to the absorptivity maxima, clearly reveal two key features: (i) A pronounced angular asymmetry, expressed as [$\alpha(\lambda, \theta) \neq \alpha(\lambda, -\theta)$], indicating a clear departure from the conventional reciprocal form of Kirchhoff's law. Such pronounced nonreciprocity originates from the anomalous Hall effect induced by the separation of Weyl nodes [48]. (ii) Narrow resonance linewidths and rainbow-free characteristics for both TM and TE polarizations. Unlike conventional FP resonators, in which the resonance wavelengths blueshift as the angle of incidence increases, a phenomenon known as the rainbow effect [8,49], the proposed structure exhibits remarkable angular stability over the angular range of 0° to 89°. Specifically, the TM emissivity peak and the TE absorptivity peak are well-maintained with minimal wavelength shifts ($\Delta\lambda_{\mathrm{TM}}/\lambda_0 < 0.73\%$ and $\Delta\lambda_{\mathrm{TE}}/\lambda_0 < 0.11\%$, respectively). Figs. 3(e)and 3(f) further displays the nonreciprocity color maps for both TM and TE polarizations. Two bright bands are symmetrically distributed about 0°, satisfying $|\eta(\lambda, \theta)| = |\eta(\lambda, -\theta)|$. Collectively, the narrowband, polarization-independent, nonreciprocal emission characteristics can not only be achieved at the initial design angle of 50°, but are also robust against angular variations, which holds considerable interest for practical applications.

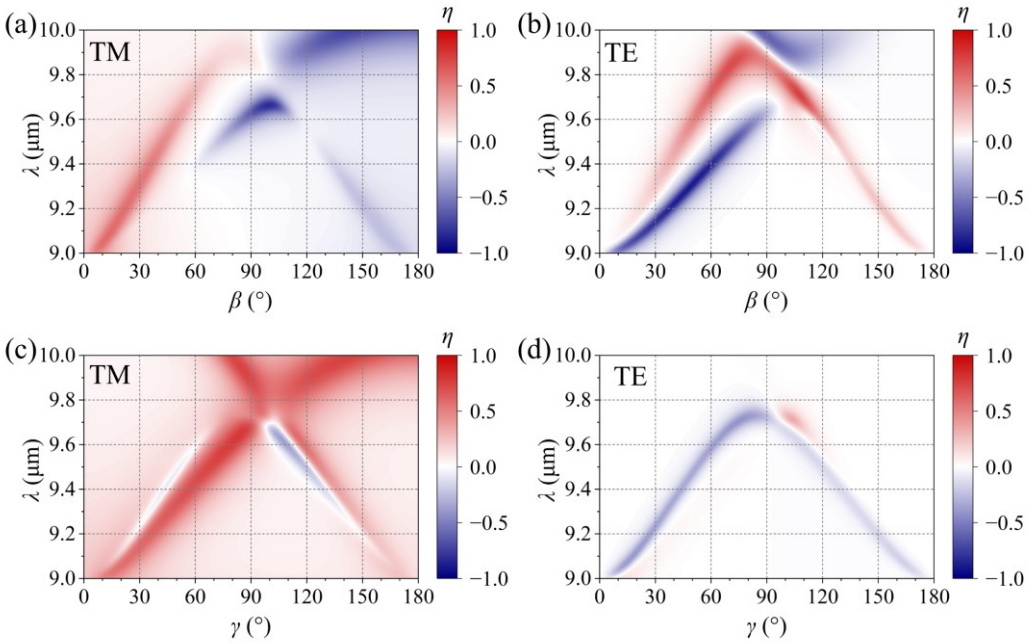


Fig. 4. Nonreciprocal thermal radiation under single-layer WSM rotation. (a) TM-polarized and (b) TE-polarized nonreciprocity as a function of wavelength λ and the rotation angle β of the upper WSM_1, with the lower WSM_2 fixed at $\gamma = 0°$. (c) TM-polarized and (d) TE-polarized nonreciprocity as a function of wavelength λ and the rotation angle γ of the lower WSM_2, with the upper WSM_1 fixed at $\beta = 0°$. Here, $\theta = 50°$, $h_1 = 0.9$ μm, $h_2 = 0.7$ μm, $h_3 = 1$ μm.

To further clarify the role of the two independently rotated WSM layers, we investigated the nonreciprocal response when only one WSM layer is rotated. As shown in Figs. 4 (a) and (b), when the lower WSM_2 is kept unrotated ($\gamma = 0°$) and the rotation angle β of the upper WSM_1 is varied from $0°$ to $180°$, although the regions of TM and TE nonreciprocity exhibit overlap, the nonreciprocity is relatively weak (e.g., η is about 0.45 when $\beta = 0°\sim20°$ and $\lambda = 9.0\mu m\sim9.1\mu m$). A similar behavior is observed when the upper WSM_1 is kept unrotated ($\beta = 0°$) and only the lower WSM_2 is rotated, as shown in Figs. 4 (c) and (d). These results indicate that a single rotation degree of freedom provides insufficient flexibility to simultaneously achieve strong and comparable nonreciprocal responses for both TM and TE

polarizations at the same wavelength. By contrast, independently rotating the two WSM layers provides two rotation angles, β and γ, which offer additional structural degrees of freedom and enable the TM and TE resonant responses to be jointly optimized. We note that previous work [24] reported TM and TE nonreciprocal thermal radiation using a twisted-WSM configuration, but their same-wavelength dual-polarization response was obtained with two distinct emitters operating at different twist angles (86° for TM and 48° for TE). In contrast, our design uses a single emitter, with the upper and lower WSM layers independently rotated by β and γ, and achieves nonreciprocity at the same wavelength. This enables polarization-independent nonreciprocal thermal radiation at a common wavelength ($\eta >$ 0.86 for both polarizations), fundamentally distinguishing our approach from the previous reports.

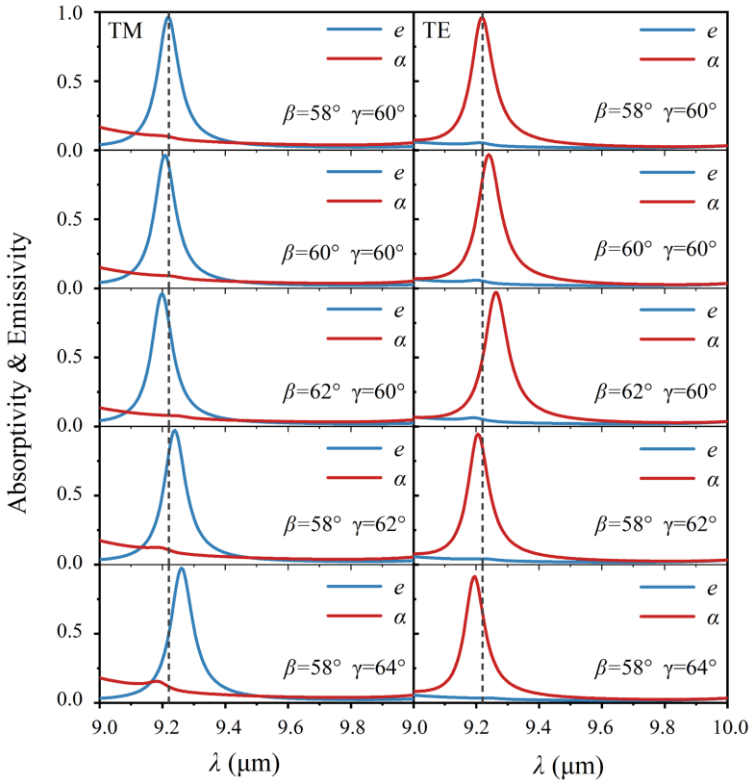


Fig. 5. Absorptivity and emissivity spectra under TM and TE polarizations for various combinations of rotation angles β and γ. The gray dashed line denotes $\lambda = 9.22\mu m$.

We investigate the effect of the rotation angles of the two WSM layers (β and γ) on the TM and TE resonance wavelengths. As shown in Fig. 4, when the other geometric parameters and the incidence angle are fixed ($\theta = 50°$), the rotation angles of the top and bottom WSM layers exert distinct effects on the resonant peaks. Specifically, increasing β while holding γ constant causes the TM resonance to blueshift and the TE resonance to redshift. Conversely, increasing γ while holding β constant produces the opposite trend: a redshift in the TM resonance and a blueshift in the TE resonance. These findings demonstrate that independently designed rotation angles β and γ provide a degree of freedom for manipulating the relative positions of TM and TE resonance wavelengths.

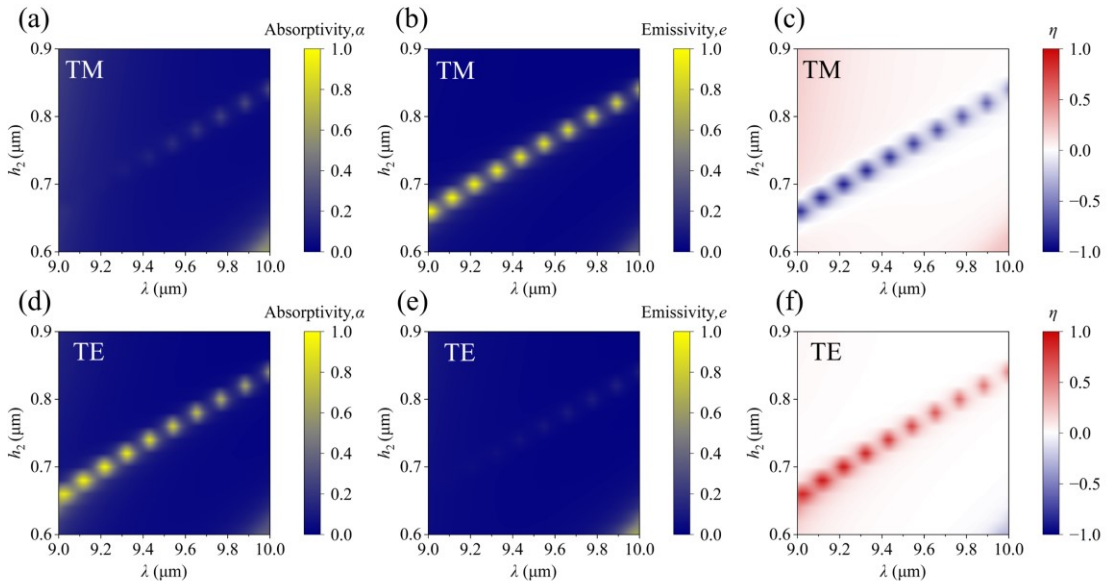


Fig. 6. Absorptivity, emissivity and nonreciprocity as a function of Si layer thickness (h_2) and wavelength λ for (a-c) TM and (d-f) TE polarizations. The parameters are set as: $h_1 = 0.9\ \mu m,\ h_3 = 1\ \mu m,\ \beta = 58°,\ \gamma = 60°,\ \theta = 50°$.

Figures 5(a-f) illustrate the influence of the Si-layer thickness (h_2) on the nonreciprocal thermal radiation response. As h_2 increases, the resonance wavelengths for both TM and TE polarizations undergo pronounced redshifts. This behavior can be readily explained by the FP resonance condition [Eq. (14)]: an increase in h_2 demands a shift toward longer resonant wavelengths to re-establish the phase matching. Remarkably, the resonant wavelengths of the two polarizations remain closely aligned over the entire range of h_2, offering a robust approach to tailoring the target wavelengths while maintaining polarization-independent characteristics.

3. Conclusion

In summary, we propose a WSM/Si/WSM/Ag Fabry–Pérot cavity emitter comprising two WSM layers with independent rotation angles. This structure successfully achieves simultaneous nonreciprocal thermal radiation for both TM and

TE polarizations at a common resonant wavelength, while maintaining angular stability ($\Delta\theta = 43°$ for TM and $\Delta\theta = 60°$ for TE). Impedance-matching analysis and field distributions are employed to elucidate the underlying physical mechanisms. In addition, the effects of the rotation angles and the Si-layer thickness on the nonreciprocal performance are systematically investigated. This work offers a novel pathway toward the high-efficiency design of nonreciprocal thermal emitters. Such polarization-independent and angular robustness are beneficial for practical thermal management and energy harvesting, where realistic illumination environments feature varying incidence angles and mixed TM- and TE-polarized radiation components.

Acknowledgments

This work is supported by National Natural Science Foundation of China (Youth Science Fund, No. 52406113), Natural Science Foundation of Ningbo (2024J429), Natural Science Foundation of Zhejiang Province (LMS25E060003), Research Start-up funds of Ningbo Innovation Center (NBGD2023X009), Key Research and Development Program of Ningbo (2024Z146), Ningbo Talent Project (2023A-392-G).

References

[1] Ying Y, Ma B, Yu J, Huang Y, Chosh P, Shen W, Qiu M, and Li Q 2022 *Laser Photonics Rev.* **16** 2200018.

[2] Xu J, Mandal J and Raman A P 2021 *Science* **372** 393-397.

[3] Shi K, Xing Y, Sun Y, He N, Guo T and He S, 2022 *Adv. Opt. Mater.* **10** 2201732.

[4] Lee M, Kim G, Jung Y, Pyun K R, Lee J, Kim B W and Ko S H 2023 *Light Sci. Appl.* **12** 134.

[5] Cho J W, Lee Y J, Kim J H, Hu R, Lee E and Kim S K 2023 *ACS nano* **17** 10442-10451.

[6] Ying Y, Yu J, Qin B, Zhao M, Zhou T, Shen W, Qiu M and Li Q 2023 *Laser Photonics Rev.* **17** 2300407.

[7] Jiang X, Yuan H, He X, Du T, Ma H, Li X, Luo M, Zhang Z, Chen H, Yu Y, Zhu G, Yan P, Wu J, Zhang Z and Yang J 2023 *Nanophotonics* **12** 1891-1902.

[8] Wang K, Sun K, Ding Q, Zeng L, Du J, Han Z, Huang L and Wang W 2025 *Nano Lett.* **25** 3613-3619.

[9] Chen Z and Hu R 2025 *Adv. Opt. Mater.* **13** e01219.

[10] Tsurimaki Y, Qian X, Pajovic S, Han F, Li M and Chen G 2020 *Phy. Rev. B* **101** 165426.

[11] Green M A 2012 *Nano Lett.* **12** 5985-5988.

[12] Shayegan K J, Zhao B, Kim Y, Fan S and Atwater H A 2022 *Sci. Adv.* **8** eabm4308.

[13] Sui J, Liao S and Zhang H 2026 *Nanophotonics* **15** e70046.

[14] Wu J, Wu B, Shi K, Wu X and Fu C 2023 *Int. J. Therm. Sci.* **187** 108172.

[15] Sun M, Qian L, Xian F, Pei S and Zheng G 2024 *Opt. Laser Technol.* **170** 110308.

[16] Wang J, Sun Y, Shi K, Zhou C, Yin Y, Shen Y and Xing X 2025 *Appl. Phys. Lett.* **127** 132201.

[17] Yu J, Zou J, Fang J, Liu T, Wang M, Sun X, Wu Y and Zhang D 2025 *J. Phys. D: Appl. Phys.* **58** 385105.

[18] Yu J, Fang J, Zou J, Liu T, Wang M, Sun X, Wu Y, Zhang D 2026 *Chin. Phys. B* **35** 094206.

[19] Fang J, Zou J, Sun Z, Liu T, Wang M, Sun X, Wu Y, Chen W and D Zhang 2024 *Int. Commun. Heat Mass Transf.* **159** 108147.

[20] Lao Y, Zhang F, Wang B and Zhou J 2026 *Int. J. Heat Mass Transf.* **267** 128918.

[21] Cao G, Guan C, Lao J, Fu J, Wu Q, Wang C, Ding X 2026 *Laser Photonics Rev.* e71619.

[22] Zhang W, Li Z, Liu T and Li W 2025 *IEEE J. Sel. Top. Quantum Electron.* **31** 4700408.

[23] Li H and Zheng G 2024 *Opt. Commun.* **550** 130002.

[24] Fang J, Zou J, Chen W, Sun X and Zhang D 2025 *J. Appl. Phys.* **138** 223102.

[25] Fang J, Zou J, Liu T, Wang M, Sun X, Wu Y and Zhang D 2024 *Appl. Phys. Lett.* **124** 171702.

[26] Shi X and Wang B 2025 *J. Mater. Chem. A* **13** 17578-17589.

[27] Do B, Nabavi B, Ghalekohneh S J, Adebiyi T, Zhao B and Zhang R 2026 *Int. J. Heat Mass Transf.* **266** 128889.

[28] Li J, Wang B and Wu J 2024 *Appl. Mater. Today* **39** 102345.

[29] Peng W, Wang B and He Y 2026 *Int. J. Heat Mass Transf.* **261** 128546.

[30] Wu J and Qing Y 2024 *Int. Commun. Heat Mass Transf.* **156** 107639.

[31] Zou H, Wang B and Wu J 2024 *Int. J. Heat Mass Transf.* **231** 125819.

[32] Guo C, Zhao B, Huang D and Fan S 2020 *ACS Photonics* **7** 3257-3263.

[33] Kotov O V and Lozovik Yu E 2018 *Phys. Rev. B* **98** 195446.

[34] Yan B and Felser C 2017 *Annu. Rev. Condens. Matter Phys.* **8** 337-354.

[35] Zhao B, Guo C, Garcia C A C, Narang P and Fan S 2020 *Nano lett.* **20** 1923-1927.

[36] Huo K, Rong M, Yang B, Wu F and Yin C 2025 *Phys. Lett. A* **535** 130282.

[37] Xu K, Zhang J, Yang B, Wu F and Yin C 2024 *Physica B* **691** 416329.

[38] Liu H, Hu Y, Ai Q, Xie M and Wu X 2022 *J. Appl. Phys.* **132** 175105.

[39] Ghalekohneh S J, Du C and Zhao B 2024 *Appl. Phys. Lett.* **124** 101104.

[40] Zhang Z and Zhu L 2023 *Phys. Rev. Appl.* **19** 014013.

[41] Xu K, Shi K, Rong M, Hu R and Yin C 2026 *Nanophotonics* **15** e70075.

[42] Zhu L and Fan S 2014 *Phys. Rev. B* **90** 220301.

[43] Shi K, Sun Y, Hu R and He S 2024 *Nanophotonics* **13** 737-747.

[44] Wang Z, Qian L, Zheng G and Wu X 2024 *Int. Commun. Heat Mass Transf.* **157** 107810.

[45] Chen Z, Yu S and Hu R 2024 *Sci. China Technol. Sci.* **67** 3285-3293.

[46] Wu J and Qing Y 2023 *Mater. Today Phys.* **32** 101025.

[47] Kats M A and Capasso F 2016 *Laser Photonics Rev.* **10** 735-749.

[48] Guo C, Asadchy V S, Zhao B and Fan S 2023 *eLight* **3** 2.

[49] Sun K, Cai Y, Huang L and Han Z 2024 *Nat. Commun.* **15** 4019.